S. Zhang,*[a] H. Hajiyani,*[b] A.G. Hufnagel,*[c,e] J. Kampmann,[c] B. Breitbach,[a] T. Bein,[c]
D. Fattakhova-Rohlfing,[d,f] R. Pentcheva,[b] C. Scheu,[a]

Sn-doped hematite for photoelectrochemical water splitting: the effect of Sn concentration

[a] Max-Planck-Institut für Eisenforschung GmbH, 40237, Düsseldorf, Germany.
[b] Department of Physics and Center for Nanointegration (CENIDE), Universität Duisburg-Essen, Lotharstraße 1, 47057 Duisburg, Germany.
[c] Department of Chemistry and Center for NanoScience (CeNS), University of Munich (LMU), Butenandtstraße 5-13 (E), 81377 Munich, Germany.
[d] Institute of Energy and Climate Research (IEK-1), Forschungszentrum Jülich GmbH, Wilhelm-Johnen-Straße, 52425 Jülich, Germany.
[e] Current Address: BASF SE, Carl-Bosch-Straße 38 67056 Ludwigshafen, Germany
[f] Faculty of Engineering and Center for Nanointegration Duisburg-Essen (CENIDE), Universität Duisburg-Essen, Lotharstraße 1, 47057 Duisburg, Germany
* These authors contributed equally to this work.

Abstract: Hematite-based photoanodes have been intensively studied for photoelectrochemical water oxidation. The *n*-type dopant Sn has been shown to benefit the activity of hematite anodes. We demonstrate in this study that Sn-doped hematite thin films grown by atomic layer deposition can achieve uniform doping across the film thickness up to at least 32 mol%, far exceeding the equilibrium solubility limit of less than 1 mol%. On the other hand, with the introduction of Sn doping, the hematite crystallite size decreases and many twin boundaries form in the film, which may contribute to the low photocurrent observed in these films. Density functional theory calculations with a Hubbard *U* term show that Sn doping has multiple effect on the hematite properties: with increasing Sn^{4+} content the Fe^{2+} concentration increases, leading to a reduction of band gap and finally to a metallic state. This goes hand in hand with an enhancement of the lattice constant.

1 Introduction

Hematite (α-Fe_2O_3) has long been studied for photoelectrochemical (PEC) water oxidation [1-16]. It has a suitable band gap of ~2.1 eV for solar light absorption, a very good absorption coefficient and an adequate band alignment to drive the demanding water oxidation reaction [2]. The fundamental limit of hematite, like many other transition metal oxides, is its poor conductivity. Both types of charge carriers, electrons and holes, are highly localized in space, and transport occurs by a phonon-assisted polaron mechanism. For *n*-type hematite photoanodes, the minority carrier hole has a diffusion length of only 2-4 nm [3] and is hence very prone to recombination. Therefore, only the photogenerated holes originating in the top few nanometers of a hematite layer can reach the interface for the water oxidation reaction. Nanostructuring hematite photoanodes [2, 4-7] is a common strategy to remedy the limited hole diffusion length by providing a shorter transport path for the photogenerated holes to reach the interface. Nevertheless, it is difficult to design nanostructures with a critical dimension matching the hole diffusion length. In addition, the conductivity may be further compromised by the surface and crystallographic defects in the bulk [6], and quantum confinement may alter the band structure and alignment [7].

Another possibility is to improve the transport properties of hematite by substituting other elements [8], such as Al, Si, Ti, Cr, Ni, Cu, Zn, Zr, Nb, Mo, Sn, Pt, as has been summarized in a previous report [9]. In a recent study, Sn doping was demonstrated to have the highest photocurrent and the lowest photovoltage onset among other commonly studied *n*-type dopants [10]. It is noteworthy that Sn has either been doped into hematite by the addition of a chemical precursor [9-12], or through diffusion from the fluorine doped tin oxide (FTO) substrate at high annealing temperatures [13-15]. In our recent study [16], we have identified two beneficial effects of Sn in the hematite lattice. Sn-doped hematite with < 20 nm thickness has been fabricated by atomic layer deposition (ALD), which is ultrathin and yet capable of absorbing 44% of the incident solar photons with an energy above the band gap. By introducing Sn doping at different locations of the films, it has been identified that Sn doping on the surface and in the ~5 nm subsurface volume have a beneficial effect on the transport properties. In combination with first principles electronic structure

calculations, Sn doping on the surface was shown to improve the interface kinetics by passivating surface trap states, while the subsurface doping was responsible for an improved charge separation by inducing a band edge gradient. Nevertheless, doping Sn throughout the thickness of the film does not translate to improved efficiency.

For screening the effect of doping elements, the doping concentration rarely exceeds 1~5 mol%. One practical constraint is the solubility of foreign atoms in the hematite structure [8]. For example, SnO_2 has a very limited solubility in hematite, less than 1 mol% below 800 ºC [17]. A higher solubility of 6 mol% [18] and 20 mol% [17] of SnO_2 has been demonstrated in hematite nanoparticles, which found applications in the gas sensor industry [17]. ALD is a powerful technique to deposit films that are far from their thermal equilibrium. In this study, we demonstrate that Sn can be incorporated into the hematite crystal structure at a concentration as high as 32 mol%. Nevertheless, the photocurrent derived from hematite photoanodes peaks at low Sn concentration, and vanishes as the Sn concentration exceeds 32 mol%.

2 Experimental

2.1 Preparation of photoanodes

The oxide films were deposited on FTO-coated glass substrates (Pilkington, 7 Ω square^{-1}), prepared by successive sonication in Extran(Merck) solution, ultrapure water (MilliQ, 18.2 MΩ cm), and 2-propanol for 15 min and drying in a stream of nitrogen. Single side polished Si(100) wafers (Siltronic AG) were used as substrates for microstructural characterization (section 2.2). Ferrocene (Aldrich, 98%) was purified by sublimation prior to use.

A Picosun R-200 Advanced ALD system was used for all depositions. The chamber temperature was 250 °C at a pressure of approximately 10 hPa. Nitrogen (Air Liquide, 99.999 %) was used at a constant flow rate of 100 sccm per precursor feed line and 150 sccm for the reactor chamber as a carrier and purge gas. Hematite was deposited by alternating between exposures to ferrocene, kept in a stainless steel cylinder at 90 °C, and ozone, produced by an INUSA AC2025 ozone generator fed with 1 vol% N_2 in O_2 (Air Liquide, 99.9995%). One full cycle consisted of a 1 s ferrocene pulse, 6 s purge, 6 s ozone pulse and a final 8 s purge. Tin oxide was deposited from tin(IV) chloride ($SnCl_4$, SAFC electronic grade) and MilliQ water, both kept in stainless steel cylinders at 18 °C. One deposition cycle consisted of a 0.1 s $SnCl_4$ pulse, 6 s purge, 15 s water pulse and final 8 s purge. Mixed oxide films were prepared interspersing one cycle of tin oxide after every N cycles of hematite, resulting in films with an ALD cycle ratio of the two oxides of 1 : N, which is used to identify samples throughout this study. This was done by alternating between N hematite deposition cycles and one tin oxide cycle until 1000 hematite cycles were reached, then capping with another N hematite cycles. A thicker pure hematite film was grown for structural characterization using 1600 cycles, consisting of a 1.5 s ferrocene pulse, 7 s static exposure and 8 s purge, followed by a 6 s ozone pulse, 7 s static exposure and 8 s purge. After deposition, the films were annealed in air at 600 °C for 30 min with a heating rate of 3.2 °C/min, and then cooled naturally to room temperature.

2.2 Microstructural Characterization

X-ray diffraction (XRD) was performed using a Rigaku SmartLab X-ray diffractometer with a Cu-Kα (1.54056 Å) radiation produced at 35 kV and 200 mA. The in-plane 2θ scan is configured using the 5- Circle goniometer with a scan speed of 2° /min and 0.12° per 2θ step. For the in-plane diffraction, both the incident and diffracted beams are nearly parallel to the sample surface, so that the penetration depth of the beam is within 100 nm of the surface. The technique measures lattice planes that are nearly perpendicular to the sample surface. Rietveld refinement was performed using the Bruker TOPAS software for the fundamental parameter fit (Pawley method). Pole figures of hematite thin films were recorded on a Seifert diffractometer with a Co-Kα (1.78897 Å) radiation produced at 40 kV and 30 mA, a parallel beam optic and an energy-dispersive point detector.

Further microstructure characterization was conducted in a Titan Themis microscope operated at 300 kV. Aberration correction of the probe-forming lenses enables a probe size of < 1 Å and a convergence semi-angle of 23.8 mrad. High angle annular dark field (HAADF) and annular bright field (ABF) micrographs were collected using annular detectors with collection semi-angles in the range of 73-200 mrad and 8-16 mrad, respectively. Energy dispersive spectroscopy (EDS) was done using a SuperX Si drift detector. Elemental quantification was performed using the Bruker Espirit

software by the standardless Cliff-Lorimer method. Electron energy loss spectroscopy (EELS) was conducted using a Gatan Quantum ERS spectrometer operated in the image-coupled mode with a collection semi-angle up to 35 mrad.

2.3 Optical Characterization

UV-Vis absorption data of hematite film electrodes was obtained on a Perkin Elmer Lambda 1050 UV/Visible/NIR spectrophotometer combined with an integrating sphere. The intrinsic absorbance of the films was calculated by applying an expression derived by Klahr et al. [19], which corrects for substrate absorption as well as substrate and film reflectance.

2.4 Photoelectrochemistry

PEC measurements were performed in a 20 cm^3 optical glass three-electrode cell with 0.1 M NaOH as the electrolyte. The oxide film was masked with poly-tetrafluoroethene adhesive tape to limit the exposed area to 0.159 cm^2, contacted with silver paste and used as the working electrode. For cyclovoltammetry (CV) measurements, the film was connected as working electrode to a Metrohm PGStat302N potentiostat. Additionally, a Pt wire (as counter electrode) and a saturated Ag/AgCl reference electrode (Sigma Aldrich, 0.197 V vs. SHE) were used to apply defined potential sweeps and to record the resulting current in a three electrode setup. CV measurements were performed at a scan rate of 20 mV s^{-1}. The applied potentials vs. RHE (V_{RHE}) were afterwards calculated from the measured at pH 13 vs. Ag/AgCl ($V_{Ag/AgCl}$) according to the following equation:

$$\left(\frac{V_{RHE} - V_{Ag/AgCl}}{V} \right) = 0.197 + 0.059 \, pH$$

The film was illuminated from the front side by a blue light emitting diode (Thorlabs, 455 nm). The flux incident on the electrode was set to be 10^{17} cm^{-2} s^{-1} at the sample position prior to each measurement using a certified Fraunhofer ISE silicon reference cell with a KG5 IR-cutoff filter.

2.5 Computational details

Density functional theory calculations were carried out with the VASP code, which uses the projected augmented wave (PAW) method, and pseudopotentials [20-23]. We also adopted the generalized-gradient approximation (GGA-PBE96) [24] for the exchange correlation functional and an effective Hubbard value U - J = 4.3 eV to describe static electronic correlations of the $3d$ states of Fe using Dudarev's approach [25]. For converged results, we used a plane-wave cut-off of 500 eV and a Monkhorst–Pack k-point mesh of $7 \times 7 \times 4$ [26]. A full relaxation of the unit cell and the ionic positions was performed until the residual forces were less than 0.01 eV $Å^{-1}$.

3 Results and Discussion

3.1 Atomic Layer Deposition of Sn-doped Hematite

3.1.1 Phase

Hematite has a trigonal structure (space group R -3 c, number 167), an isostructure to corundum (α-Al_2O_3). The hexagonal unit cell is conventionally used, so are the hexagonal Miller-Bravais indices (h, k, i, l) to label the diffraction. We use the full 4 indices in this manuscript, whereas most studies omit the dummy index $i = - h - k$. Note however, the rhombohedral index also uses 3 indices, but they are defined using the rhombohedral unit cell. The conversion between the 2 systems of the low-index lattice planes is listed in Table 1.

XRD characterization was conducted on the ultrathin hematite films grown on flat Si(100) substrates. A fiber texture has been demonstrated for undoped hematite [16] with the plane normal of Fe_2O_3 (0,0,0,6) (c-plane) parallel to the growth direction. In order to maximize the signal from the ultrathin films, we applied the in-plane diffraction geometry with grazing incidence, while collecting diffractions only from planes 90° to the growth direction due to the fiber

texture. As shown in Table 1 and Fig. 1a, the peaks observed in this geometry are all in-plane reflections, including (1,1,-2,0), (3,0,-3,0), and (2,2,-4,0).

Tab. 1: Conversion between the hexagonal Miller-Bravais index and the rhombohedral index of the low-index hematite planes, and their inclination angles to the (0,0,0,6) plane normal (growth direction of the fiber textured film). The in-plane reflections are highlighted in bold.

| 2θ (°)	Plane spacing (Å)	Hexagonal index	Rhombohedral index	Inclination to the growth direction (°)
24.0	3.70	(0,1,-1,2)	(1,1,0)	58
33.0	2.71	(1,0,-1,4)	(2,1,1)	38
35.4	2.53	**(1,1,-2,0)**	**(1,0,-1)**	**90**
39.0	2.30	(0,0,0,6)	(2,2,2)	0
40.6	2.22	(1,1,-2,3)	(2,1,0)	61
43.3	2.09	(2,0,-2,2)	(2,0,0)	72
49.2	1.85	(0,2,-2,4)	(2,2,0)	58
53.7	1.70	(1,1,-2,6)	(3,2,1)	42
57.1	1.61	(1,2,-3,2)	(2,1,-1)	77
57.2	1.61	(0,1,-1,8)	(3,3,2)	22
62.1	1.49	(2,1,-3,4)	(3,1,0)	64
63.6	1.46	**(3,0,-3,0)**	**(2,-1,-1)**	**90**
69.1	1.36	(2,0,-2,8)	(4,2,2)	38
71.5	1.32	(1,0,-1,10)	(4,3,3)	18
71.8	1.31	(1,1,-2,9)	(4,3,2)	31
75.0	1.27	**(2,2,-4,0)**	**(2,0,-2)**	**90**
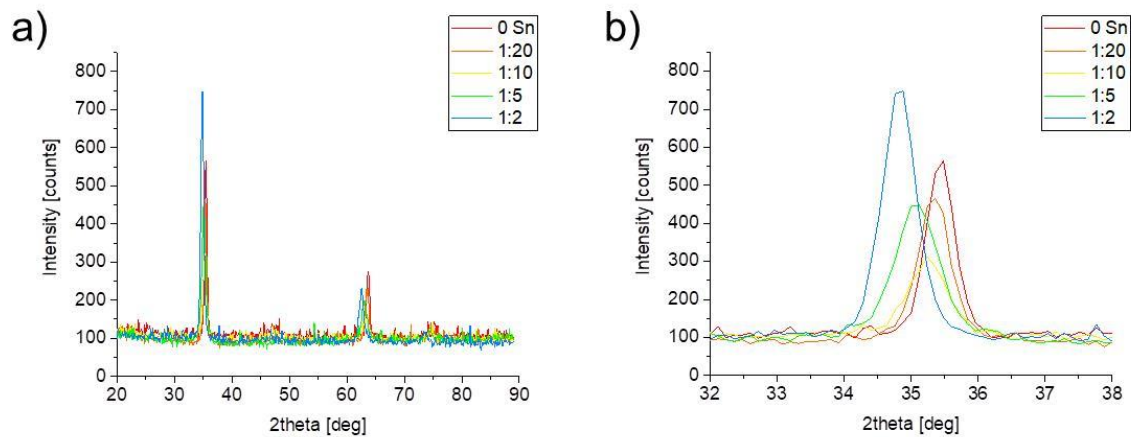
Fig. 1: (a) In-plane XRD of Sn-doped hematite with various ALD cycle ratios and (b) the enlarged view on the (1,1,-2,0) reflection.

As the concentration of Sn increases, no new reflections have been identified. This may suggest the absence of crystalline phases other than hematite, but cannot exclude crystalline phases with a different texture and hence not contributing to in-plane diffraction. The (1,1,-2,0) reflection shifts to the left monotonically as the Sn concentration increases, indicating an expansion of the lattice parameter a, which is summarized in Table 2.

3.1.2 Chemical composition

The chemical composition of the thin films and their homogeneity were studied by EDS and EELS in STEM. It has been noted in our earlier study [28] that due to the fluorescence artefact of Sn from the FTO substrate, EDS is inappropriate to quantify small amount of Sn in the hematite thin film. In this study, we quantify Sn in the hematite films grown on the Si(100) substrate so that the fluorescence artefact is no longer a concern. As shown in Table 2, the Sn concentration increases as the ALD cycle ratio of 1 cycle of SnO_2 per N cycles of Fe_2O_3 (abbreviated 1: N) increases, i.e., tin oxide layers are separated by fewer layers of iron oxide. A high Sn concentration of 32 mol% is reached at the ratio of 1:5, approximating to the chemical formula $SnFe_2O_x$. Even at this composition, a homogeneous distribution of Fe and Sn throughout the film thickness is evidenced in Fig.2b, and there is no indication of a second phase. With the Sn concentrations evaluated by EDS, the expansion of the in-plane lattice parameter a is evaluated as 0.03% per mol% of Sn. This is comparable to the evaluation from Sn-doped hematite nanoparticles [17] where both lattice parameters a and c expand 0.02% per mol% of Sn.

Tab. 2: Summary of Sn-doped hematite thin films with various ALD cycle ratios: Chemical composition (EDS), lattice parameters (XRD), chemical shift of Fe-L_3 edge (EELS) and the deducted Fe^{2+} concentration.

ALD cycle ratio	Sn (mol%)	a (Å)	Fe-L_3 edge (eV) *	Fe^{2+} (mol%)
0	0	5.0629 ± 0.0006	710.22 ± 1.37	0
1:20	6	5.0766 ± 0.0007	710.12 ± 1.47	6
1:10	14	5.0893 ± 0.0013	710.08 ± 1.74	8
1:5	32	5.1129 ± 0.0010	710.02 ± 1.57	12

* The notation ± in this column does not refer to uncertainty, rather the width (1 standard deviation) of the peak from a Gaussian profile fitting
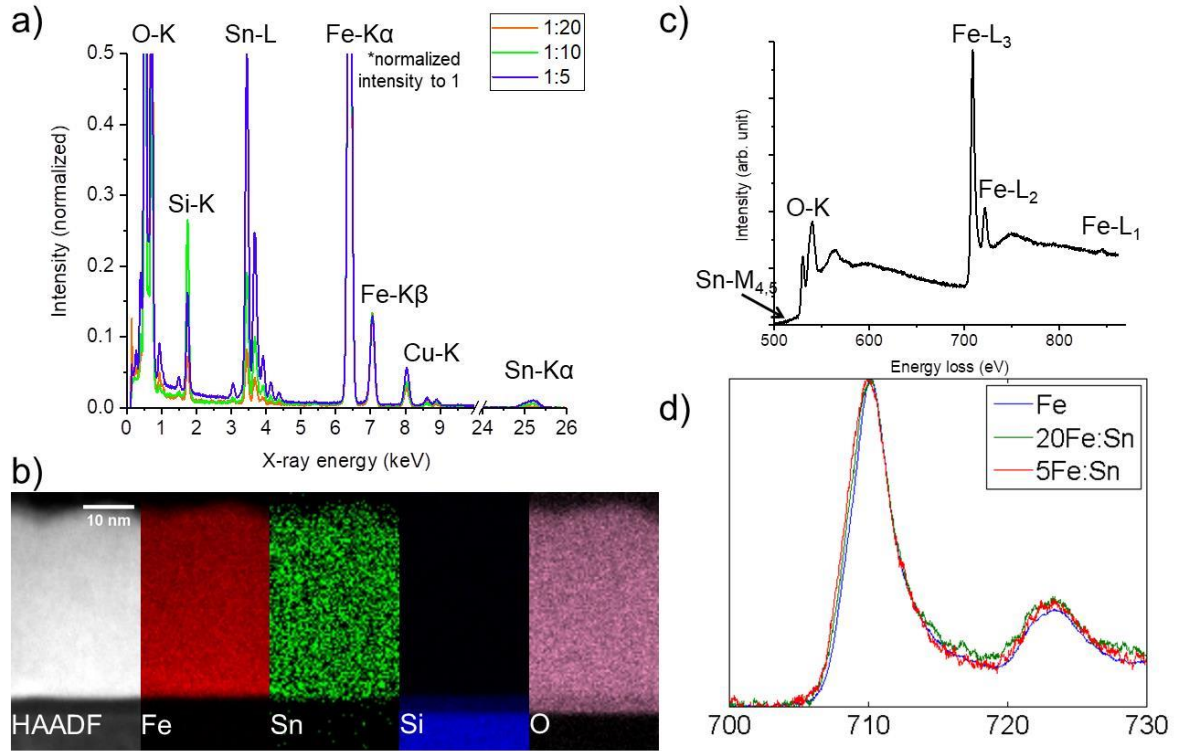

Fig. 2: (a) EDS spectra of Sn-doped hematite thin films with various ALD cycle ratios and (b) EDS elemental maps of the film with ALD cycle ratio 1:5. (c) EELS spectrum of the film with ALD cycle ratio 1:20 and (d) the chemical shift of the Fe-L_3 edge between undoped hematite and Sn-doped hematite with ALD cycle ratio 1:5.

The incorporation of Sn is further evidenced by its effect on the oxidation state of Fe. As discussed in a previous work, a shift of the EELS Fe-L_3 edge (Fig. 2c) towards lower energy loss corresponds to the reduction of Fe^{3+} [28]. Integrating the EELS spectra from within Sn-doped hematite, a monotonic shift of Fe-L_3 position is observed towards lower energy loss. This is in agreement with theoretical studies [9, 16] that suggest that Fe atoms adjacent to substitutional Sn^{4+} atoms can be reduced to a Fe^{2+} state. In Sn-doped hematite, the Fe L_3 edge is a superposition of the Fe^{3+} and Fe^{2+} spectra. Hence, a shift of the peak centroid towards lower energy loss is expected together with a broadening of the profile, as shown in Fig. 2c and Table 2. Fe^{3+} and Fe^{2+} minerals were characterized to have a 1.7 eV difference in the Fe-L_3 position [29]. The fraction of Fe^{2+} ions was then linearly interpolated using their peak chemical shift. As shown in Table 2, Fe^{2+} concentration increases more mildly as the Sn concentration in hematite increases.

3.1.3 Theoretical understanding from DFT+U calculations

To gain insight into the effect of higher Sn concentrations on the properties of hematite we have performed density functional theory calculations with a Hubbard U parameter. Three different Sn concentrations were selected: 8.33, 16.67 and 33.33 mol%. The most stable cation configurations, the electronic properties including oxidation states of iron and the evolution of lattice parameters with Sn-concentration are displayed in Fig. 3. In our previous work [16], we have shown that doping with a single Sn^{4+} in the 30-atom α-Fe_2O_3 unit cell (8 mol% doping, which is close to the experimental value of 6 mol% in Table 2) turns Fe^{3+} in the neighbouring cation layer to Fe^{2+}. A similar effect was previously observed also for Ti-doped hematite [27]. The additional $3d$-electron forms a localized band just below the Fermi-level (cf. density of states in Fig. 3a). Analysis of oxidation states and electronic properties in Fig. 3b-c shows that further increase of the Sn amount leads to a corresponding enhancement of the Fe^{2+} concentration (in line with the experimental measurement in Tab. 2) and reduction of the band gap. At 17 mol% Sn in Fig. 3b, the localized band of one of the Fe^{2+} ions is close to the conduction band minimum. At 33 mol%, the Fermi level crosses the conduction band minimum and leads to n-type conductivity. The DFT+U calculations render a monotonic increase of the lattice parameters and the volume (cf. Fig. 3d), the latter showing a linear increase, whereas the dependence of a/c flattens/becomes steeper with increasing concentration. Overall the DFT+U values are higher than in the experiments, likely due to the overestimation of lattice parameters typical for the GGA-PBE96 exchange correlation functional together with a Hubbard U correction. Moreover, while we have considered here substitutional doping of Sn, other mechanisms such as incorporation at other sites and the formation of cation vacancies may also play a role.
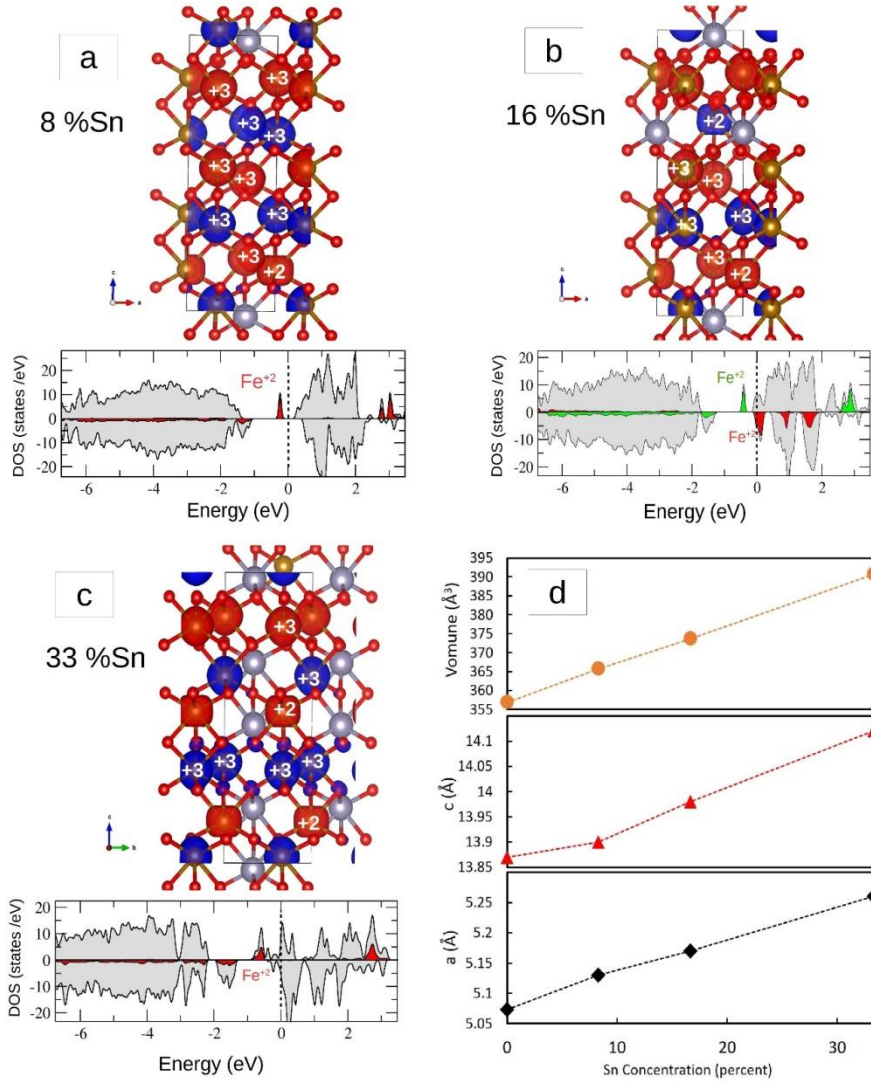
Fig. 3: Side view and spin density of Sn-doped hematite with Sn concentration of a) 8, b) 17, and c) 33 mol%. Fe^{3+} sites (d^5) possess a nearly spherical spin density, whereas at the Fe^{2+} sites (d^6) it is flattened. The corresponding density of states shows a reduction of the band gap due to localized states in the gap related to the sixth electron at Fe^{2+}. At 33 mol% Sn, the Fermi level crosses the conduction band leading to *n*-type conductivity. d) Volume and lattice parameters of hematite as a function of Sn concentration.

3.2 Crystallinity of ALD Sn-doped hematite

In addition to the phase determination, we have applied XRD to study the crystallinity of the hematite thin films. It is noteworthy that in-plane diffraction is not suitable to quantify crystallinity as the grazing incidence geometry makes the measurement very sensitive to the surface alignment and its area. In our previous study [16], we have relied on the Bragg-Brentano geometry (θ-2θ scans) to evaluate the crystallinity, as well as out-of-plane pole figure measurements. As shown in the (1,0,-1,4) pole figures (Fig. 4), an apparent fiber texture is only observed in the hematite films without and with 6 mol% Sn. For the higher Sn concentrations, the pole figures become noisier, suggesting a decrease in the crystallinity.
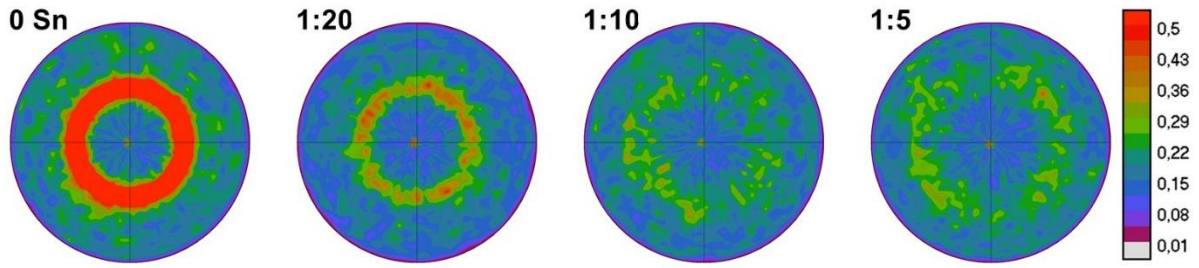
Fig. 4: XRD (1,0,-1,4) pole figures of Sn-doped hematite thin films with various ALD cycle ratios.

In real space, the decrease in crystallinity is manifested by the decrease in grain sizes. As shown in the STEM micrograph (Fig. 5a), the hematite thin films have columnar grains, and each grain has a vertical size equal to the film thickness. The surface termination is a (0,0,0,6) plane as evident in Fig.5b, 5c, which is in agreement with the XRD texture measurement. For the Sn-doped sample, however, many grains no longer span from the substrate to the surface, as shown by the highlighted grains in Fig. 5d, 5g. Moreover, it is observed that many hematite grains have a twin relationship. As an example, Fig. 5e shows the left and right grains in a twin relationship, whereas the middle part of the micrograph captures an overlapped area with both orientations. It is clear from the fast Fourier transform (FFT) pattern in Fig. 5f that the twins have the mirror symmetry on the (0,0,0,6) as well as the (3,0,-3,0) planes. Finally, for the high Sn concentration at 32 mol%, even smaller hematite grains are observed. As the grain size is much below the thickness of the specimen, it is difficult to observe these grains in atomic resolution. Nevertheless, twins are evidenced by the FFT pattern in Fig. 5i. As a common defect in hematite, twins are formed by dehydration of α-FeOOH [30], having a coherent boundary and a common oxygen sublattice.

Despite their chemical homogeneity, it is clear that the grains are smaller in the hematite films with higher Sn concentrations. This may be understood by the ALD process where the hematite layer deposition is more frequently interrupted by the SnO_2 deposition to realize higher Sn concentration. Nevertheless, the observed grain size is much bigger than the thickness of hematite deposition between the SnO_2 deposition (< 1 nm). The calcination procedure is a determining factor to the crystallinity. A mild calcination temperature of 600 ºC for 30 min was chosen for this set of samples, which has been demonstrated to promote short-range (~1 nm) diffusion to homogenize the Sn doping as well as to inhibit longer range diffusion [16]. While serviceable for designing localized Sn doping profiles, such calcination does not result in highly crystallized films at higher Sn concentrations. Higher calcination temperatures up to 800 ºC [13-15] have been reported to produce hematite thin film photoanodes on FTO substrates. Under these circumstances, however, Sn was found to diffuse into the hematite even from the FTO substrate [13, 15].

Long range diffusion may also cause unwanted Sn segregation as Sn has a low solubility in Fe_2O_3 [17]. In a recent study on hematite sintered at 1300 ºC [31], Sn was demonstrated to segregate at the grain boundaries between the sintered particles. We have previously demonstrated that a pure hematite underlayer can promote the crystalline growth of Sn-doped hematite on top [16].
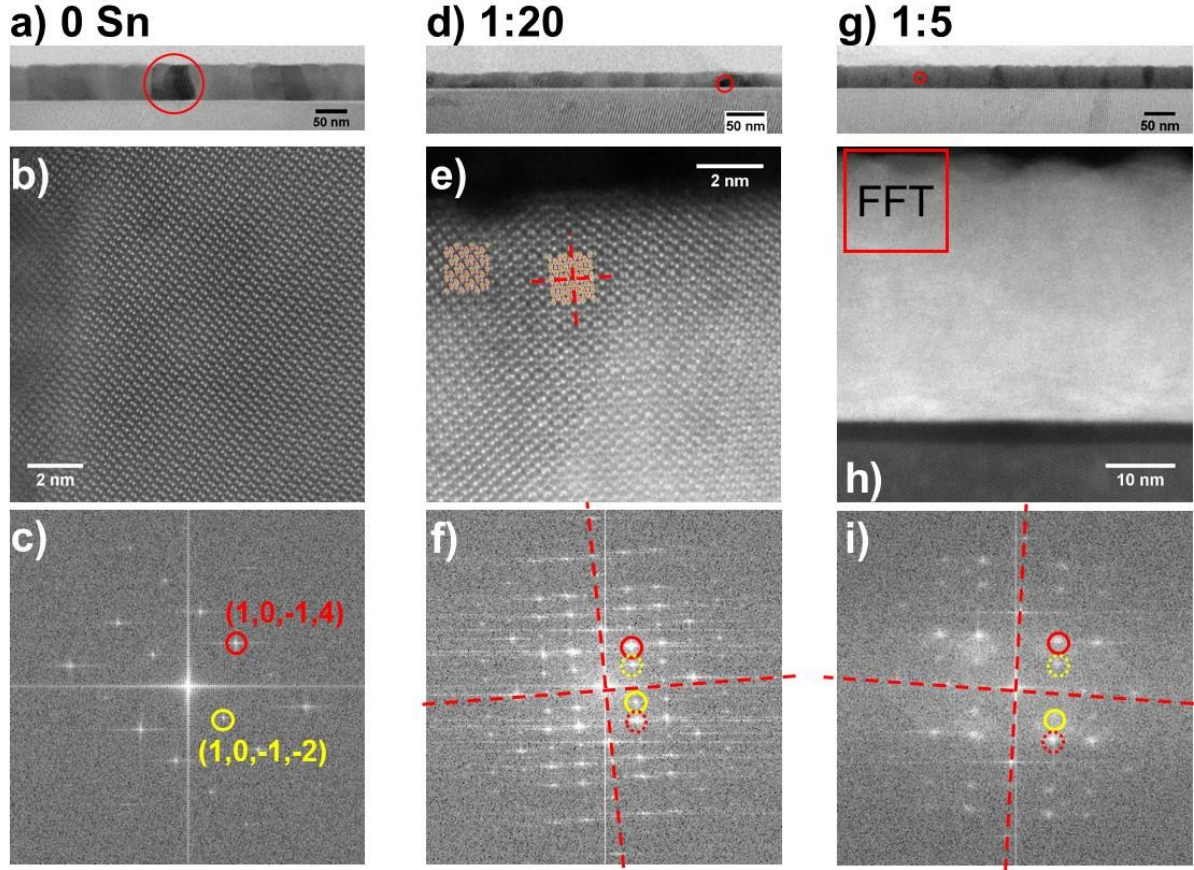
Fig. 5: STEM images of hematite films **(a,b,c)** without Sn doping, **(d,e,f)** with 6 mol% Sn (ALD cycle ratio 1:20), and **(g,h,i)** with 32 mol% Sn (ALD cycle ratio 1:5). The first row shows ABF-STEM images to identify some individual grains as highlighted by the red circles. The second row shows atomic resolution HAADF-STEM images along the [1,-2,1,0] zone axis of hematite grains and twin boundaries. The atomic structure of hematite and an overlaid twin are superimposed in the grain and twin boundary areas in **(e)**. The third row shows the FFT of their corresponding HAADF-STEM images with (1,0,-1,4) and (1,0,-1,-2) reflections marked by circles in red and yellow, and their twin variants marked by broken circles in their respective colors. The broken lines in **(e,f,i)** highlights the mirror symmetry of the twin.

Overall, we have observed that the crystallinity of the hematite phase decreases as the Sn concentration increases. This compares well with the behaviour of ultrathin hematite films grown on FTO substrates [16].

3.3 Photoelectrochemical Water Splitting

To evaluate any correlation between the Sn concentration and the PEC performance, we characterized the hematite thin film electrodes by cyclovoltammetry (CV) measurements in the dark and under illumination (Fig. 6b, see experimental part for further information). Furthermore, we used the CV data to calculate the photocurrent density at 1.23 V vs. RHE (by subtraction of the dark current density at this potential from the respective current density under illumination) for all different doping levels to elucidate the optimal Sn concentration, which peaks at a SnO_2/Fe_2O_3 ALD cycle ratio of 1:100 (Fig. 6c). Significant differences in the obtained current densities under illumination can be observed. In the case of low SnO_2/Fe_2O_3 ALD cycle ratios (1:40, 1:80, 1:100, 1:120, 1:150), we see an improvement over undoped hematite which can be attributed to both improved electrical conductivity and charge separation properties. [9, 12, 16] On the other hand, the opposite was observed for higher Sn concentrations (SnO_2/Fe_2O_3 ALD cycle ratios of 1:20, 1:10, 1:5), as the recorded current density is reduced compared to the undoped hematite electrode, especially for the highest Sn concentration.
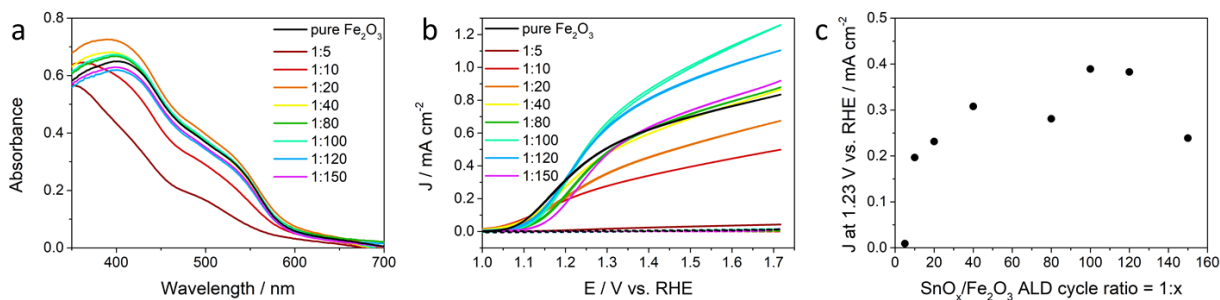
Fig. 6: (a) Absorbance data of hematite photoanode films on FTO with different Sn concentrations used for PEC experiments. Films with high Sn concentrations (ALD cycle ratios 1:10 and 1:5) show a significantly lower absorbance below 600 nm compared to lower doping concentrations. (b) CV measurements of Sn-doped hematite photoanodes with varied Sn concentration (colored) compared to an undoped hematite film (black). The difference between the current under illumination (solid lines) and the dark current (respective dashed lines) is proportional to the water oxidation activity. (c) The calculated photocurrent density at 1.23 V vs. RHE, which was calculated from the current density under illumination subtracted by the dark current density at this potential, which peaks at the ALD cycle ratio of 1:100.

As discussed in Sec. 3.2, the grain size of hematite decreases as the Sn concentration increases from 6 to 32 mol%. Crystallographic defects, including grain boundaries, are known to form trap states for charge carriers. Especially for hematite, a material known for slow hole transport, grain boundaries have been demonstrated to cause carrier recombination [6]. Additionally, our oxide films with high SnO_2/Fe_2O_3 ALD cycle ratios of 1:10 and 1:5 showed a significantly decreased optical absorbance of light in the visible range (Fig. 6a). Therefore, we attribute the diminished PEC performance to both inferior crystallinity and a reduced absorbance with rising Sn content.

4 Conclusions

We present a study on the effect of Sn concentration on the microstructure and PEC water oxidation activity of hematite photoanodes. It is demonstrated that by ALD, up to 32 mol% Sn can be homogeneously incorporated into the hematite phase. The photocurrent peaks at an ALD cycle ratio of 1:100, whereas the photocurrent vanishes for a ratio of 1:5, which corresponds to 32 mol% Sn in hematite. The DFT+U results show that an increase of Sn concentration leads to an enhancement of Fe^{2+} which reduces the bandgap down to an n-type metallic state at 33 mol%. The theoretical results also confirm the increase of the lattice constants with Sn concentration. In addition, we found that the crystallinity of the hematite thin film decreases with increasing Sn concentration, which is correlated to the observation of twin boundaries. The increase of grain boundary density may explain the reduction in PEC activity. Nevertheless, this metastable film may find other applications making use of the lattice expansion and other solid solution effects.

5 Acknowledgment

6 References

[1] K.L. Hardee and A.J. Bard, J. Electrochem. Soc., 1976, 123, 1024.

[2] K. Sivula, F. Le Formal and M. Grätzel, ChemSusChem, 2011, 4, 432.

[3] J.H. Kennedy and K.W. Frese Jr., J. Electrochem. Soc., 1978, 125, 709.

[4] R. van de Krol, Y. Liang and J. Schoonman, J. Mater. Chem., 2008, 18, 2311.

[5] A. Kay, I. Cesar and M. Grätzel, J. Am. Chem. Soc., 2006, 128, 15714.

[6] U. Björksten, J. Moser and M.Grätzel, Chem. Mater., 1994, 6, 858.

[7] L. Vayssieres, C. Sathe, S.M. Butorin, D.K. Shuh, J. Nordgren and J. Guo, Adv. Mater., 2005, 17, 2320.

[8] R. Shinar and J.H. Kennedy, Solar Energy Mater., 1982, 6, 323.

[9] A. Mettenbörger, Y. Gönüllü, T. Fischer, T. Heisig, A. Sasinska, C. Maccato, G. Carraro, C. Sada, D. Barreca, L. Mayrhofer, M. Moseler, A. Held and S. Mathur, Nano Energy, 2016, 19, 415.

[10] K. D. Malviya, H. Dotan, D. Shlenkevich, A. Tsyganok, H. Mor and A. Rothschild, J. Mater. Chem. A, 2016, 4, 3091.

[11] N.T. Hahn and C.B. Mullins, Chem. Mater., 2010, 22, 6474.

[12] H.K. Dunn, J.M. Feckl, A. Müller, D. Fattakhova-Rohlfing, S.G. Morehead, J. Roos, L.M. Peter, C. Scheu and T. Bein, Phys. Chem. Chem. Phys., 2014, 16, 24610.

[13] Y. Ling, G. Wang, D.A. Wheeler, J.Z. Zhang and Y. Li, Nano Lett. 2011, 11, 2119.

[14] C.D. Bohn, A.K. Agrawal, E.C. Walter, M.D. Vaudin, A.A. Herzing, P.M. Haney, A.A. Talin, V.A. Szalai, J. Phys. Chem. C, 2012, 116, 15290.

[15] B. Wickman, A. Bastos Fanta, A. Burrows, A. Hellman, J.B. Wagner and B. Iandolo, Sci. Rep. 2017, 7, 40500.

[16] A.G. Hufnagel, H. Hajiyani, S. Zhang, T. Li, O. Kasian, B. Gault, B. Breitbach, T. Bein, D. Fattakhova-Rohlfing, C. Scheu and R. Pentcheva, Adv. Funct. Mater., 2018, 28, 1804472.

[17] M. Takano, Y. Bando, N. Nakanishi, M. Sakai and H. Okinaka, J. Solid State Chem., 1987, 68, 153.

[18] J.Z. Jiang, R. Lin, S. Morup, K.Nielsen, F.W. Poulsen, F.J. Berry, R. Clasen, Phys. Rev. B, 1997, 55, 11.

[19] B. M. Klahr, A. B. Martinson and T. W. Hamann, *Langmuir* 2011, 27, 461.

[20] G. Kresse and J. Hafner, Phys. Rev. B 1994, 49, 14251.

[21] G. Kresse and J. Furthmüller, Comput. Mater. Sci. 1996, 6, 15.

[22] G. Kresse and J. Furthmüller, Phys. Rev. B 1996, 54, 11169.

[23] P. Blöchl, Phys. Rev. B 1994, 50, 17953.

[24] J. P. Perdew, K. Burke and M. Ernzerhof, Phys. Rev. Lett. 1996, 77, 3865.

[25] S. L. Dudarev, G. A. Botton, S. Y. Savrasov, C. J. Humphreys and A. P. Sutton, Phys. Rev. B 1998, 57, 1505.

[26] H. J. Monkhorst and J. D. Pack, Phys. Rev. B 1976, 13, 5188.

[27] R. Pentcheva and H. Sadat Nabi, Phys. Rev. B 2008, 77, 172405.

[28] S. Zhang and C. Scheu, Microscopy, 2018, 67, i133.

[29] P.A. van Aken and B. Liebscher, Phys. Chem. Miner. 2002, 29, 188.

[30] F. Watari, J. van Landuyt, P. Delavignette, S. Amelinckx and N. Igata, Phys. Stat. Sol. A, 1982, 73, 215.

[31] M.R.S. Soares, C.A.R. Costa, E.M. Lanzoni, J. Bettini, C.A.O. Ramirez, F.L. Souza, E. Longo and E.R. Leite, Adv. Electr. Mater., 2019, 1900065.